Binary mask optimization for forward lithography based on the boundary layer model in coherent systems

Xu Ma* and Gonzalo R. Arce

Department of Electrical and Computer Engineering, University of Delaware, Newark, Delaware 19716, USA
**Corresponding author: maxu@udel.edu*

Received March 9, 2009; revised May 20, 2009; accepted May 23, 2009;
posted May 27, 2009 (Doc. ID 108443); published June 24, 2009

Recently, a set of generalized gradient-based optical proximity correction (OPC) optimization methods have been developed to solve for the forward and inverse lithography problems under the thin-mask assumption, where the mask is considered a thin 2D object. However, as the critical dimension printed on the wafer shrinks into the subwavelength regime, thick-mask effects become prevalent, and thus these effects must be taken into account in OPC optimization methods. OPC methods derived under the thin-mask assumption have inherent limitations and perform poorly in the subwavelength regime. This paper focuses on developing model-based forward binary mask optimization methods that account for the thick-mask effects of coherent imaging systems. The boundary layer (BL) model is exploited to simplify and characterize the thick-mask effects, leading to a model-based OPC method. The BL model is simpler than other thick-mask models, treating the near field of the mask as the superposition of the interior transmission areas and the boundary layers. The advantages and limitations of the proposed algorithm are discussed, and several illustrative simulations are presented.

OCIS codes: 220.3740, 100.3190, 110.1650.

1. INTRODUCTION

Due to the resolution limits of optical lithographic systems, the electronics industry has relied on resolution enhancement techniques (RETs) to compensate and minimize mask distortions as they are projected onto semiconductor wafers [1]. Resolution in optical lithography obeys the Rayleigh resolution limit $R=k(\lambda/NA)$, where λ is the wavelength, NA is the numerical aperture, and k is the process constant that can be minimized through RET methods [2–5]. In optical proximity correction (OPC), mask amplitude patterns are modified by the addition of subresolution features that can precompensate for imaging distortions.

Several approaches to forward and inverse lithography have been proposed in the literature. Sherif *et al.* derived an iterative approach to generate binary masks in incoherent diffraction-limited imaging systems [6]. Liu and Zakhor developed a binary and phase-shifting mask (PSM) design strategy based on the branch and bound algorithm and simulated annealing [7]. Pati and Kailath developed suboptimal projections onto convex sets for PSM designs [8]. In addition, Erdmann *et al.* proposed automatic optimization of the mask and illumination parameters with a genetic algorithm [9]. Pang *et al.* gave an overview of inverse lithography technology (ILT) and provided some simulations to demonstrate the benefit of ILT [10]. Granik described and compared solutions of inverse mask problems [11].

Poonawala and Milanfar developed a pixel-based optimization framework for inverse lithography, well suited for gradient-based search [12]. Ma and Arce generalized this algorithm so as to admit multiphase components having arbitrary PSM patterns [13,14]. However, both of the algorithms focus on the coherent illumination system. Recently, Ma and Arce used the sum-of-coherent-systems (SOCS) model and the average coherent approximation model to develop effective and computationally efficient binary mask design algorithms for inverse lithography under partially coherent illuminations [15,16]. Subsequently, Ma and Arce developed a PSM design algorithm based on a sigular value decomposition (SVD) model under partially coherent systems [17,18]. In addition, they extended their work to allow for the joint optimization of the source and the mask [19].

All of the algorithms above, however, have been developed under the thin-mask assumption, where Kirchhoff's boundary condition is directly applied to the mask topology and consequently the mask is treated as a 2D object [20,21]. As the critical dimension (CD) printed on the wafer shrinks into the subwavelength regime, the thick-mask effects become very pronounced such that these effects should be taken into account in the mask optimization. Thick-mask effects include polarization dependence due to the different boundary conditions for the electric and magnetic fields, transmission error in small openings, diffraction edge effects or electromagnetic coupling, and so on [20]. The thick-mask effects can be rigorously represented by the near-field pattern of the mask, which is different from the Kirchhoff approximation of the mask topography. Two decades ago, Wong and Neureuther discovered the intensity imbalance of alternating PSM, and applied the finite-difference time-domain (FDTD) method to study the mask topography effects in the projection printing of the PSM [22,23]. This phenom-

enon was proved by experimental results later [24]. Yuan exploited the waveguide (WG) method to model the light diffraction of 2D phase-shifting masks [25], which was subsequently generalized by Lucas to the 3D topography [26]. Erdmann, *et al.* evaluated and compared the FDTD method and the WG method for the simulation of typical hyper *NA* ($NA>1$) imaging problem [27]. Adam and Neureuther introduced domain decomposition methods for the simulation of photomask scattering [28]. Nevertheless, these approaches are too complex to be applied in model-based binary mask design.

Recently, Azpiroz *et al.* introduced a novel boundary layer (BL) model for fast evaluation of the near field of a thick mask [20,21]. Different from other computationally complex and resource consuming rigorous mask models, the BL model treats the near field of the mask as the superposition of the interior transmission areas and the boundary layers, which have fixed dimensions and determined locations. The BL model effectively compensates for the inaccuracy of Kirchhoff's approximation, which is attributed to thick-mask effects, different polarizations, and phase errors. The simplicity and accuracy of the BL model enables the formulation of a model-based optimization algorithm for binary masks. This paper thus focuses on the formulation of a model-based forward binary mask optimization algorithm based on the BL model to take into account the thick-mask effects under coherent illumination. This is accomplished as follows: First, the optical lithography process under coherent illumination is formulated as the combination of the BL model and the Hopkins diffraction model. The cost function of the binary mask optimization problem is formulated as the square of the l^2-norm of the difference between the real aerial image and the desired pattern on the wafer. Then the gradient of the cost function, referred to as the cost sensitivity function, is developed and used to drive the cost function in the descent direction during the optimization process. Topological constraints of the binary mask are introduced and used to limit the minimum opening size of the optimized mask pattern.

The remainder of the paper is organized as follows: The Hopkins diffraction model of optical lithography systems is summarized in Section 2. The BL model of coherent imaging system is summarized in Section 3. The lithography preliminaries and the cost sensitivity function are developed in Section 4. The binary mask optimization algorithm based on the BL model under coherent illumination is described in Section 5. Simulation results are illustrated in Section 6. Conclusions are provided in Section 7.

2. HOPKINS DIFFRACTION MODEL OF THE OPTICAL LITHOGRAPHY SYSTEM

According to the Hopkins diffraction model, the light intensity distribution exposed on the wafer, referred to as the aerial image under partially coherent illumination (PCI), is bilinear and is described by [29]

$$I(\mathbf{r}) = \int\int M^*(\mathbf{r_1})M(\mathbf{r_2})\gamma(\mathbf{r_1}-\mathbf{r_2})h^*(\mathbf{r}-\mathbf{r_1})h(\mathbf{r}-\mathbf{r_2})\mathrm{d}\mathbf{r_1}\mathrm{d}\mathbf{r_2}, \tag{1}$$

where $\mathbf{r}=(x,y)$, $\mathbf{r_1}=(x_1,y_1)$ and $\mathbf{r_2}=(x_2,y_2)$. $M(\mathbf{r})$ is the mask pattern, $\gamma(\mathbf{r_1}-\mathbf{r_2})$ is the complex degree of coherence, and $h(\mathbf{r})$ represents the amplitude impulse response of the optical system. The amplitude impulse response $h(\mathbf{r})$ is defined as the Fourier transform of the circular lens aperture with cutoff frequency NA/λ [30,31]; therefore,

$$h(\mathbf{r}) = \frac{J_1(2\pi rNA/\lambda)}{2\pi rNA/\lambda}. \tag{2}$$

The complex degree of coherence $\gamma(\mathbf{r_1}-\mathbf{r_2})$ is generally a complex number, whose magnitude represents the extent of optical interaction between two spatial locations $\mathbf{r_1}=(x_1,y_1)$ and $\mathbf{r_2}=(x_2,y_2)$ of the light source [1]. The complex degree of coherence in the spatial domain is the inverse 2-D Fourier transform of the illumination shape. In general, this equation is tedious to compute, both analytically and numerically [32]. The system reduces to simple forms in the two limits of complete coherence or complete incoherence. For the completely coherent case, the illumination source is at a single point, thus, $\gamma(\mathbf{r})=1$. In this case, the aerial image in Eq. (1) is separable on $\mathbf{r_1}$ and $\mathbf{r_2}$, and thus

$$I(\mathbf{r}) = |M(\mathbf{r}) \otimes h(\mathbf{r})|^2, \tag{3}$$

where $\otimes$ is the convolution operation. For the completely incoherent case, the illumination source is of infinite extent, and thus $\gamma(\mathbf{r})=\delta(\mathbf{r})$. In this case, the aerial image reduces to

$$I(\mathbf{r}) = |M(\mathbf{r})|^2 \otimes |h(\mathbf{r})|^2. \tag{4}$$

This paper focuses on the binary mask optimization based on the BL model under coherent illumination. A schematic of an optical lithography system with coherent illumination is illustrated in Fig. 1.

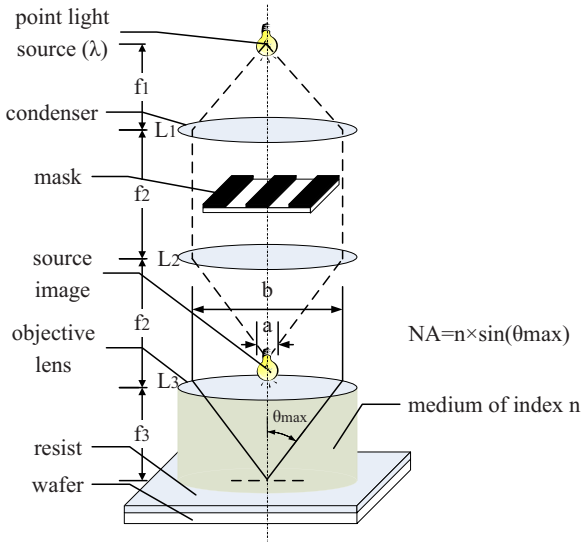

Fig. 1. (Color online) Optical lithography system with coherent illumination.

3. BOUNDARY LAYER MODEL

The Kirchhoff approximation has been extensively used in the development of OPC methods, where the mask thickness is assumed to be infinitesimal and the mask is considered a 2D object. As the CD printed on the wafer shrinks into the subwavelength regime, however, the thick-mask effects become significant and thus need to be taken into account in the design of OPC methods. Although numerous rigorous mask models simulating the 3D electromagnetic field of the mask have been developed, these models are resource-consuming and too complex to be applied in the model-based binary mask design for forward lithography.

A. Boundary Layer Model of Coherent Imaging

Recently, Azpiroz *et al.* introduced a novel BL model for fast evaluation of the near-field of the thick mask, where the near field is modeled as the superposition of the interior transmission areas and the boundary layers with fixed dimensions and determined locations [20,21]. The concepts of the BL model under coherent illumination are illustrated in Fig. 2, where the polarization of the impending electric field **E** is assigned to be in the horizontal direction. Figure 2 shows a typical rectangular opening of the binary mask with width equal to a and height equal to b. The harmonic mean of the area's width a and height b is $d=2ab/(a+b)$. The near field of the opening is divided into five areas: A, B, C, D and E. A is the interior transmission area with transmission coefficient $\eta_I=1$ for the binary mask. The transmission coefficients of the boundary layers depend on the polarization of the electric field of the impending light. Since the polarization of the electric field is assigned to be in the horizontal direction, B and D are the tangential boundary areas with width w and transmission coefficient η_T. C and E are the normal boundary areas with width w and transmission coefficient η_N. In the BL model, the relative error of amplitude of the electric field on the wafer produced by the thin-mask approximation is measured by the deviation of its real component from the EM field value rigorously calculated with the FDTD method. Experimental results show that the relative error of amplitude is in proportion to the width of the boundary layer w and inversely proportional to the harmonic mean d, represented as

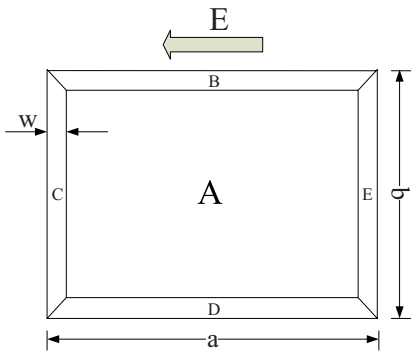

Fig. 2. (Color online) BL model under coherent illumination, where the polarization of the electric field is assigned to be in the horizontal direction. w is the width of the boundary areas; a and b are the width and height, respectively, of the entire opening area.

$$Re\left\{\frac{\Delta\mathbf{E}}{\mathbf{E}}\right\}=\frac{4w}{d}=\frac{(2a+2b)w}{ab}=\frac{Boundary\ Layer\ Area\ (real\ part)}{Total\ Area}, \quad (5)$$

where $Re\{\cdot\}$ denotes the real part of the argument, $\mathbf{E}$ is the total electric field from the Em field value rigorously calculated with the FDTD method, $\Delta\mathbf{E}$ is the electric field error from the thin-mask assumption, and $Re\{\Delta\mathbf{E}/\mathbf{E}\}$ is the the relative error of amplitude. Given a and b, w can be calculated from Eq. (5). The deviation of the real component is compensated by the opaque boundary layers surrounding all openings on the mask, whose transmission coefficients are zero. Given the value of w, it is shown experimentally that the relative error of phase is in proportion to w and transmission coefficient $|\eta_T|$ and inversely proportional to the height of the opening b, represented as

$$Im\left\{\frac{\Delta\mathbf{E}}{\mathbf{E}}\right\}=|\eta_T|\frac{2w}{b}=|\eta_T|\frac{2aw}{ab}=|\eta_T|\frac{Boundary\ Layer\ Area\ (imaginary\ part)}{Total\ Area}, \quad (6)$$

where $Im\{\cdot\}$ denotes the imaginary part of the argument. Subsequently, the relative error of phase is compensated by the boundary layers with complex transmission coefficient η_T and width w on the opening edges tangent to the electric field of the impinging light. The inaccuracy of the thin-mask approximation is effectively offset by the superposition of complex-valued boundary layers. The real values of the boundary layers are zero (opaque) around the area A. The complex values are η_T in the tangential direction and zero in the normal direction. These values for η_T and η_N have been shown in [20,21] to effectively compensate for the thin-mask distortion. The transmission coefficient of the tangential boundary areas, η_T, is calculated from the slope of the linear relation described in Eq. (6). However, the relationships described in Eqs. (5) and (6) are not accurate when the opening size decreases below the wavelength. For the BL model to be valid, the minimum size of the opening must be constrained to be larger than the wavelength. The simplicity and accuracy of the BL model are suitable for the model-based binary mask optimization algorithms.

Azpiroz *et al.* [20,21] studied two types of optical lithography systems. The first one is a 4× projection system with $NA=0.68$ and $\lambda=248$ nm, while in second one $NA=0.85$ and $\lambda=193$ nm. For the first type of optical lithography system, $w=24.8$ nm, $\eta_T=0.0i$, $\eta_N=0$, and the minimum allowed opening size on the mask (the width of the area A) is 248 nm. For the second type, $w=14.5$ nm, $\eta_T=0.8i$, $\eta_N=0$, and the minimum allowed opening size is 200 nm. In our work, we will use the two types of lithography systems described by Azpiroz *et al.* to develop binary mask optimization algorithms.

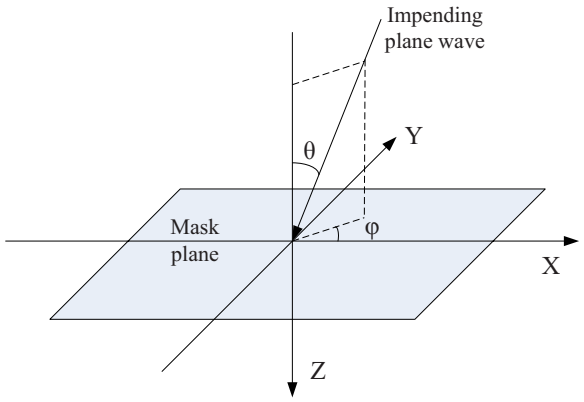

Fig. 3. (Color online) Each source point of the partially coherent illumination generates a plane wave impending on the mask plane with incident azimuth angle ϕ and elevation angle θ.

B. Boundary Layer Model of Partially Coherent Imaging

Most practical illumination sources have a nonzero line width, and their radiation is more generally described as partially coherent. In contrast to coherent illumination having a deterministic polarization, partially coherent illumination consists of an unpolarized source. For the unpolarized source, the field polarization varies randomly, and the field components generated by different source points are not correlated and are added incoherently [33]. Assume that each source point of the partially coherent illumination generates a plane wave impinging on the mask plane with incident azimuth angle ϕ and elevation angle θ, as shown in Fig. 3. It is shown in Fig. 4(a) that the unpolarized source can be modeled by the superposition of two linearly polarized plane waves, which are mutually orthogonal and normal to the propagation direction [30]. The polarization directions of the electric fields corresponding to the TE ($\hat{\mathbf{e}}_{TE}$) and TM ($\hat{\mathbf{e}}_{TM}$) modes are calculated as

$$\hat{\mathbf{e}}_{TE} = -\sin\phi\hat{\mathbf{p}}_X + \cos\phi\hat{\mathbf{p}}_Y, \tag{7}$$

$$\hat{\mathbf{e}}_{TM} = \sin\theta\cos\phi\hat{\mathbf{p}}_X + \sin\theta\cos\phi\hat{\mathbf{p}}_Y - \cos\theta\hat{\mathbf{p}}_Z, \tag{8}$$

where $\hat{\mathbf{p}}_X$ and $\hat{\mathbf{p}}_Y$ are the unit vectors along the P_X and P_Y axes, and $\hat{\mathbf{p}}_Z = \hat{\mathbf{p}}_X \times \hat{\mathbf{p}}_Y$.

When the incident elevation angle is small, the Hopkins approximation can be used to model the partially coherent illumination. In this case, the oblique impending plane wave is assumed equal to the normal impending wave except for the corresponding frequency shift. As illustrated in Fig. 4(b), based on the Hopkins approximation, the TE and TM modes of the unpolarized source can be approximated to have constant directions along the P_X and P_Y axes [33,34]. Therefore, the BL model of partially coherent illumination is approximated as the superposition of the BL model in the coherent imaging system contributed by each source point. For the on-axis source point, the BL model parameters are described in Subsection 3.A. For the off-axis source point, these boundary layer parameters have also been proven to lead to accurate results in the 4× optical lithography system with partial coherence factor $\sigma \in [0.3, 0.6]$ [33].

4. LITHOGRAPHY PRELIMINARIES AND COST SENSITIVITY FUNCTION

This section focuses mainly on the problem formulation of the binary mask optimization in the coherent imaging system. Let $M(x,y)$ be the input binary mask to an optical lithography system $T\{\cdot\}$ with coherent illumination. The system $T\{\cdot\}$ includes two steps. The first step is the evaluation of the near field of the thick mask, which is based on the BL model. The second step is the optical imaging system leading to the aerial image on the wafer, which is approximated by the Hopkins diffraction model. The output aerial image on the wafer is denoted as $Z(x,y) = T\{M(x,y)\}$. Given a $N \times N$ desired output pattern $\tilde{Z}(x,y)$, the goal of OPC mask design is to find the optimized $M(x,y)$ called $\hat{M}(x,y)$ such that the distance

$$D = d(Z(x,y), \tilde{Z}(x,y)) = d(T\{M(x,y)\}, \tilde{Z}(x,y)) \tag{9}$$

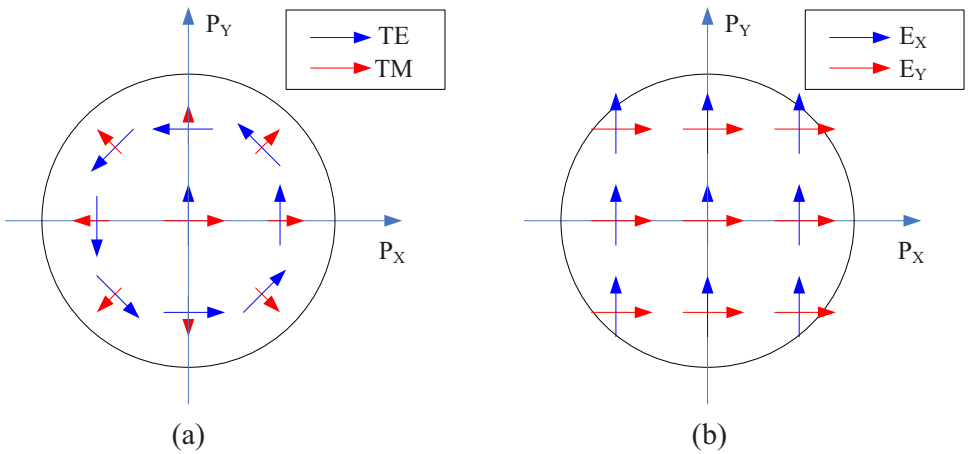

Fig. 4. (Color online) (a) Source polarization modes of TE and TM. (b) Approximated source polarization modes of E_X and E_Y (redrawn based on Fig. 4.11 in [33]).

is minimized, where $d(\cdot,\cdot)$ is the square of the l^2-norm criterion. The OPC optimization problem can thus be formulated as the search for $\hat{M}(x,y)$ over the $N\times N$ real space $\Re^{N\times N}$ such that

$$\hat{M}(x,y) = \underset{M(x,y)\in\Re^{N\times N}}{\operatorname{argmin}} d(T\{M(x,y)\},\tilde{Z}(x,y)). \quad (10)$$

The forward imaging process is illustrated in Fig. 5. The electric field propagating through the thick-mask pattern is affected by the 3D topography of the mask, forming the near field, which is then influenced by diffraction and mutual interference in the optical imaging system. Light that is transmitted through the optical system reaches the photoresist and forms the aerial image. In Fig. 5, $|\cdot|$ is the element-by-element absolute operation, and the output of the convolution and the absolute operation model is the intensity distribution of the aerial image.

Following the definitions above, the following notation is used:

(1) The $M_{N\times N}$ matrix represents the mask pattern, with entry values equal to 0 or 1 for the binary mask. The $N^2\times 1$ equivalent raster scanned vector representation is denoted as $\underline{m}$.

(2) The $\Gamma_{N\times N}(M)$ matrix, with all entry values equal to 0 or 1, represents the interior transmission area pattern of the near field corresponding to the mask M. Its vector representation is denoted as $\underline{\gamma}$.

(3) The $\Gamma\uparrow$ and $\Gamma\downarrow$ represent the shifted version of Γ by shifting Γ along the vertical direction (up and down, respectively) by one pixel. Their vector representations are denoted as $\underline{\gamma}\uparrow$ and $\underline{\gamma}\downarrow$.

(4) The $\tilde{F}_{N\times N}(M)$ matrix represents the near field corresponding to the mask M, with complex entry values. Its vector representation is denoted as $\underline{f}$. Let the polarization of the impinging electric field **E** be in the horizontal direction. For the binary mask in the first type of optical lithography system, all the BLs are opaque, with transmission coefficient 0. In order to represent all the features on the mask by an integral number of pixels, the pixel size is assigned equal to the greatest common divisor between the BL width and the minimum opening size; thus, the pixel size is set to be 24.8 nm. The minimum opening size is 248 nm=$10\times$*pixel size*. Thus, the near field is the same as the interior transmission area. Therefore,

$$\underline{f}_p = \underline{\gamma}_p, \qquad p = 1,2,\ldots,N^2. \quad (11)$$

For the binary mask in the second type of optical lithography system, the normal BLs are opaque and the tangential BLs have complex transmission coefficient of $0.8i$. The pixel size is set to be 14.5 nm. In order to represent the minimum opening size by an integral number of pixels, the minimum opening size is increased to be 203 nm $=14\times$*pixel size*. Therefore

$$\underline{f}_p = \begin{cases} 0.8j: & (\underline{\gamma}_{p-N}=1 \text{ and } \underline{\gamma}_p=0) \text{ or } (\underline{\gamma}_{p+N}=1 \text{ and } \underline{\gamma}_p=0) \\ \underline{\gamma}_p: & \text{otherwise} \end{cases}. \quad (12)$$

Equation (12) can be rewritten as

$$\underline{f}_p = 0.8j(1-\underline{\gamma}_p)\underline{\gamma}_{p-N} + 0.8j(1-\underline{\gamma}_p)\underline{\gamma}_{p+N} + \underline{\gamma}_p,$$

$$p = 1,2,\ldots,N^2, \quad (13)$$

where $\underline{\gamma}_p=0$, if $p<1$ or $p>N^2$.

(5) A convolution matrix H is an $N^2\times N^2$ matrix with an equivalent 2D filter h.

(6) The desired $N\times N$ binary output pattern is denoted as $\tilde{Z}$. It is the desired aerial image sought on the wafer. Its vector representation is denoted as $\underline{\tilde{z}}$.

(7) The initial interior transmission area of the optimization process is $\tilde{Z}$. The corresponding initial mask pattern is $\tilde{M}$.

(8) The output aerial image is the $N\times N$ matrix denoted as

$$Z = |H\{F\}|^2. \quad (14)$$

The equivalent vector is denoted as $\underline{z}$.

(9) The optimized mask denoted as $\hat{M}$ minimizes the distance between Z and $\tilde{Z}$; i.e.,

$$\hat{M} = \underset{M}{\operatorname{argmin}}\, d(|H\{F\}|^2,\tilde{Z}). \quad (15)$$

Given the output aerial image $\underline{z}=|H\{\underline{f}\}|^2$, the pth entry in this vector can be represented as

$$z_p = \left|\sum_{q=1}^{N^2} h_{pq}\underline{f}_q\right|^2, \qquad p = 1,\ldots N^2, \quad (16)$$

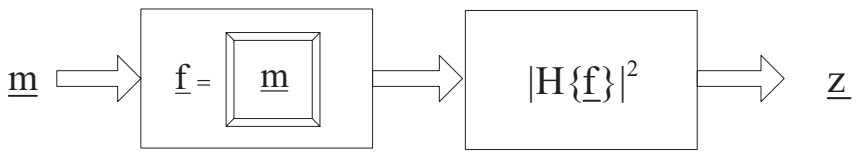

Mask | Near field evaluation based on the BL model | Convolution approximation of image formation process | Output aerial image

Fig. 5. Approximated forward imaging process based on the BL model under coherent illumination, where the polarization of the electric field is assigned to be in the horizontal direction.

where h_{pq} is the (p,q)th entry of the filter. The cost function is the l^2-norm of the difference between $\underline{z}$ and $\underline{\tilde{z}}$. Therefore,

$$D = \|\underline{\tilde{z}} - \underline{z}\|_2^2 = \sum_{p=1}^{N^2} (\tilde{z}_p - z_p)^2, \tag{17}$$

where z_p in Eq. (17) is represented in Eq. (16).

The performance of the OPC optimization algorithm is evaluated by the output pattern error, which is defined as D in Eq. (17). According to Eq. (17), the output pattern error results from the comparison between the desired pattern and the aerial image without threshold. Thus Eq. (17) does not account for the photoresist effect. It has been proven that ignoring the photoresist effect may improve the aerial image contrast [35].

In the following, the sensitivity of the cost function D with respect to the change of the interior transmission area will be used to guide the optimization process. The sensitivity of the cost function D is $\partial D/\partial \underline{\gamma}$. For the first type of optical lithography system,

$$\partial D/\partial \underline{\gamma} = -H^T[(\underline{\tilde{z}} - \underline{z}) \odot H(\underline{\gamma})], \tag{18}$$

where T is the conjugate transposition and $\odot$ is the element-by-element multiplication operation. For the second type of optical lithography system,

$$\begin{aligned}\partial D/\partial \underline{\gamma} = -4\, Re\{&H^T[(\underline{\tilde{z}} - \underline{z}) \odot H(\underline{f})] \odot (0.8i\,\underline{\gamma}\uparrow + 0.8i\,\underline{\gamma}\downarrow + 1) \\ &+ H^T[(\underline{\tilde{z}} - \underline{z}) \odot H(\underline{f})]\downarrow \odot 0.8i(1 - \underline{\gamma}\downarrow) \\ &+ H^T[(\underline{\tilde{z}} - \underline{z}) \odot H(\underline{f})]\uparrow \odot 0.8i(1 - \underline{\gamma}\uparrow)\},\end{aligned} \tag{19}$$

where $Re\{\cdot\}$ denotes the real part of the argument; $\uparrow$ and $\downarrow$ are shifting operations by shifting the $N \times N$ equivalent matrix of the vector in the argument along the vertical direction (up and down, respectively) by one pixel.

The proposed OPC optimization framework in this section is developed for coherent imaging systems and can be extended for partially coherent imaging systems. As described in Subsection 3.B, the BL model under partially coherent illumination is approximated as the superposition of the BL model in coherent imaging system contributed by each source point. Thus, the partially coherent imaging system can be decomposed into the superposition of several coherent imaging systems based on the SOCS model [29]. The near-field on the exiting surface, contributed by each coherent component, can be evaluated by the BL model in coherent imaging system. The overall near field is the superposition of the near field resulted from all coherent components. Given the overall near field, the aerial image projected on the wafer under partially coherent illumination can be calculated using the SOCS model. Following the derivation in this section, the OPC optimization problem can be formulated in a partially coherent imaging system. However, this extension is out of the scope of this paper and will be performed in future work.

5. BINARY MASK OPTIMIZATION ALGORITHM BASED ON THE BL MODEL UNDER COHERENT ILLUMINATION

A. Topological Constraint

According to the BL model summarized in Section 3, the interior transmission area has a one-to-one correspondence to the mask. Therefore, the proposed OPC mask design algorithm directly optimizes the interior transmission area, from which the mask can be easily reconstructed. The BL model constrains the minimum size of the openings on the binary mask [20,21]. In order to meet the requirements, some topological constraints are imposed in the optimization process of the interior transmission area [36,37]. In the following, some definitions and operations for shape topologies are listed.

Definition 1 (white block and black block). Any pixel in the interior transmission area can have a value of either 0 or 1. A white block is a square area with all pixels values equal to 1, while a black block has all of its pixels equal to 0.

Definition 2 (flipping-on and flipping-off operations). Turning a pixel value from 0 to 1 and from 1 to 0 are referred to as flipping-on and flipping-off a pixel. In general, flipping-on and flipping-off operations of a block means to turn the block into a white block and into a black block.

Definition 3 (type I singular pixel). A type I singular pixel is one that does not belong to any $L \times L$ white block on the interior transmission area pattern Γ, where L depends on the minimum opening size of the BL model.

Definition 4 (type II singular pixel). A type II singular pixel is one that does not belong to any 3×3 black block on the interior transmission area pattern Γ. Since the openings on the optimized binary mask contain more surrounding boundary layers than the corresponding interior transmission areas, the type II singular pixel introduces the merging of adjacent openings on the mask.

Definition 5 (cost sensitivity matrix of a block). The cost sensitivity function corresponding to a block G on the interior transmission area pattern, calculated by Eq. (18) or Eq. (19), is $\nabla D(G)$ defined as the cost sensitivity matrix of the block G.

Definition 6 (changeable block). A $K \times K$ changeable block is a block whose cost sensitivity matrix contains K positive or negative values. If the cost sensitivity matrix contains K positive values, the block is defined as a positive changeable block, and vice versa. Note that a block may be both positive and negative changeable blocks at the same time.

In our binary mask optimization approach, only the positive or negative changeable blocks are considered to be flipped-off or flipped-on. These topological constraints guarantee that the features of the optimized binary mask are larger than the minimum opening size.

B. Binary Mask Optimization Algorithm Based on the BL Model under Coherent Illumination

Following the topological constraints, the proposed binary mask optimization algorithm is described in the following, where the parameters K in **Step 3** and L used in *Definition 3* depend on the minimum opening size of the BL model.

Step 1: Initialization of the interior transmission area pattern: $\tilde{\Gamma}=\tilde{Z}$. The corresponding initial mask pattern is $\tilde{M}$.
Step 2: Calculate the cost sensitivity function using Eq. (18) and (19).
Step 3: Scan the cost sensitivity matrix from top to bottom and from left to right. Find the first encountered $K\times K$ changeable block G.
Step 4: Flip-on or flip-off G if it is a negative or positive changeable black.
Step 5: If (flipping operation has introduced type I or type II singular pixel)
flag=1.
Step 6: If (flag=1) or (cost function D is increased) or (any pixel value $\neq 0$ or 1)
restore G to its original values.
Step 7: Clear the cost sensitivity matrix of G: $\nabla D(G)=\mathbf{0}$.
Step 8: If $\nabla D\neq\mathbf{0}$
Go to step 3.
Otherwise
If no block is flipped in the current iteration
End.
Otherwise
Go to step 2.

6. SIMULATIONS

To prove the efficiency of the proposed algorithm, the optimization method described in Subsection 5.B is used to design a mask targetting the desired aerial image shown in Fig. 6. In Fig. 6, p is the pitch width. For the first type of optical lithography system, $p=49.6$ nm, and the system parameters are $NA=0.68$ and $\lambda=248$ nm. Since the system is a 4× projection system, the pitch width of the initial interior transmission area pattern $\tilde{\Gamma}$ of the optimization process is 198.4 nm. In the simulation, the initial mask pattern has the dimension of 4.56 μm×4.56 μm. The pixel size is 24.8 nm×24.8 nm, which is the same as the boundary width. The convolution kernel shown in Eq. (2) is assumed to vanish outside the area A_{h1} defined by $x,y\in[-248\text{ nm},248\text{ nm}]$. The parameters of the optimization algorithm are $K=L=8$. The simulations results using the algorithm depicted in Subsection 5.B for the first type of optical lithography system are shown in Fig. 7. The top row (from left to right) shows the initial mask pattern and the corresponding output aerial image, with output pattern error of 2791.2. Middle row (from left to right) shows the optimized binary mask using the algorithm depicted in Subsection 5.B based on thin-mask approximation and the corresponding output aerial image, with output pattern error of 1975.4. The bottom row (from left to right) shows the optimized binary mask based on the BL model and the corresponding output aerial image, with output pattern error of 1868.9. Black and white represent 0 and 1, respectively. It is shown that optimization of the binary mask based on the thin-mask approximation reduces the output pattern error by 29.2%, while the algorithm based on the BL model reduces the output pattern error by 33.0%.

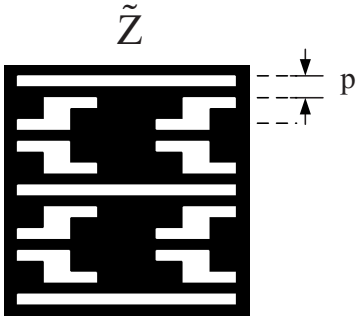

Fig. 6. Desired pattern of the aerial image searched on the wafer.

For the second type of optical lithography system, $p=43.5$ nm, the system parameters are $NA=0.85$ and $\lambda=193$ nm. The pitch width of the initial interior transmission area pattern $\tilde{\Gamma}$ of the optimization process is 174 nm. In the simulation, the initial mask pattern has the dimen-

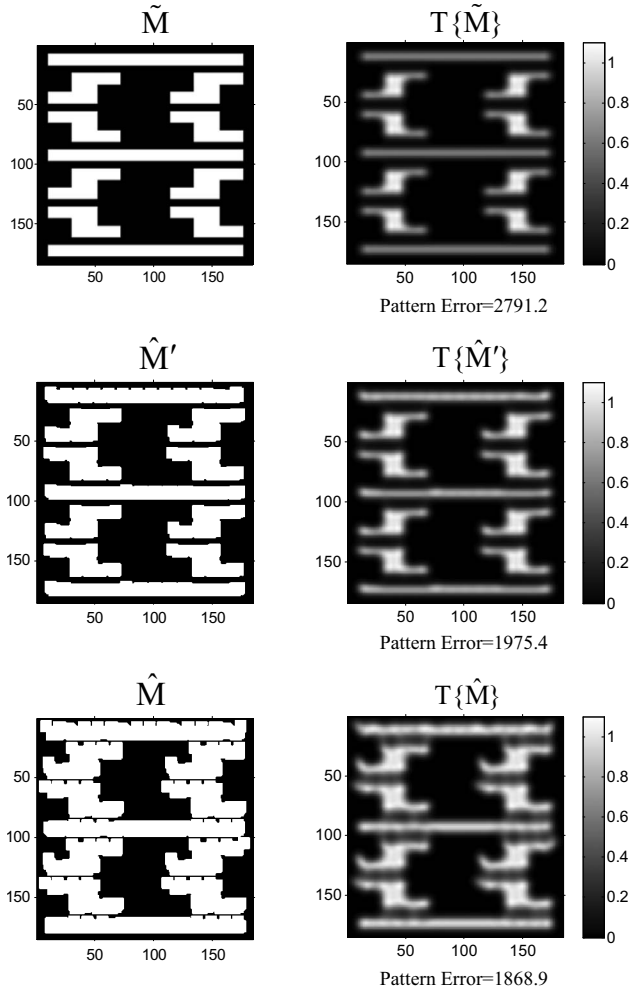

Fig. 7. Binary mask optimization based on the BL model for the first type of coherent optical lithography system. $\lambda=248$ nm. Top row (from left to right), the initial mask pattern and the corresponding output aerial image. Middle row (from left to right), the optimized binary mask based on the thin-mask approximation and the corresponding output aerial image. Bottom row, (from left to right) the optimized binary mask based on the BL model and the corresponding output aerial image. Black and white represent 0 and 1, respectively.

sions $4.00\ \mu m \times 4.00\ \mu m$. The pixel size is 14.5 nm $\times 14.5$ nm, which is the same as the boundary width. The convolution kernel is assumed to vanish outside the area A_{h2} defined by $x,y \in [-290\ \text{nm}, 290\ \text{nm}]$. The parameters of the optimization algorithm are $K=L=12$. The simulations results for the second type of optical lithography system are shown in Fig. 8. The top row (from left to right) shows the initial mask pattern and the corresponding output aerial image, with output pattern error of 7926.9. The middle row (from left to right) shows the optimized binary mask using the algorithm depicted in Subsection 5.B based on the thin-mask approximation and the corresponding output aerial image, with output pattern error of 7766.5. The bottom row (from left to right) shows the optimized binary mask based on the BL model and the corresponding output aerial image, with output pattern error of 6897.4. Black and white represent 0 and 1, respectively. It is shown that optimization of the binary mask based on the thin-mask approximation reduces the output pattern error by 2.0%, while the algorithm based on the BL model reduces the output pattern error by 13.0%. As shown in Figs. 7 and 8, the proposed binary mask optimization algorithm effectively reduces the output pattern errors and obtains more desirable aerial images. The performance differences between the optimizing mask based the on thin-mask approximation and BL model show the necessity that the proposed algorithms take into account the thick-mask effect. These results are consistent with those obtained in other simulations with different desired patterns.

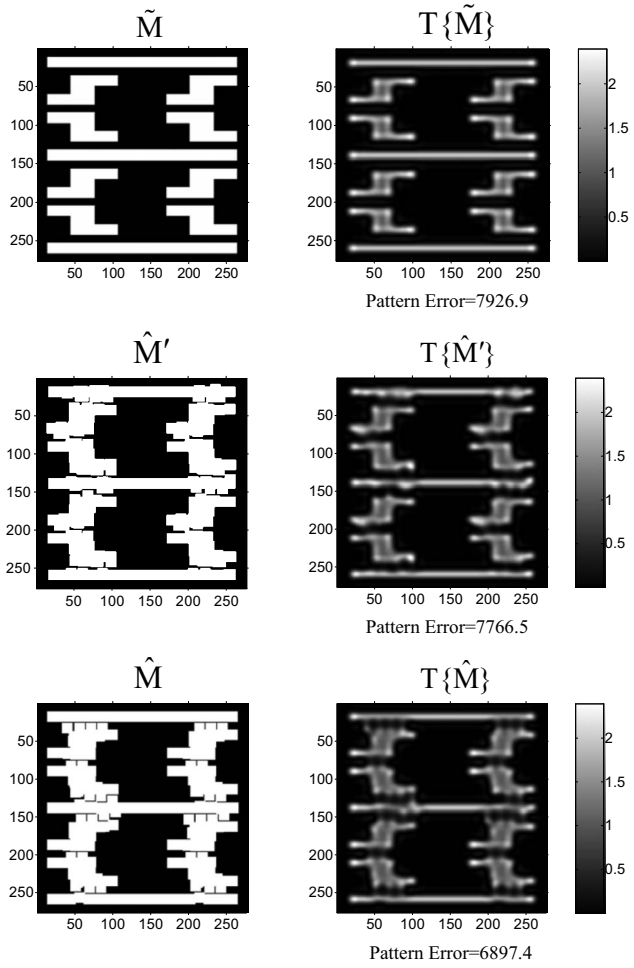

Fig. 8. Binary mask optimization based on the BL model for the second type of coherent optical lithography system. $\lambda = 193$ nm. Top row (from left to right), the initial mask pattern and the corresponding output aerial image. Middle row (from left to right), the optimized binary mask based on the thin-mask approximation and the corresponding output aerial image. Bottom row (from left to right), the optimized binary mask based on the BL model and the corresponding output aerial image. Black and white represent 0 and 1, respectively.

For both of the simulations above, the computation was done on an Intel Pentium4 CPU, 3.40 GHz, 1.0 GB of RAM. Matlab is used as the software platform to program and perform the OPC optimization.

7. CONCLUSION

This paper studies binary mask optimization for model-based forward lithography taking into account the thick-mask effects under coherent illumination. The BL model is applied to evaluate the near field of the thick mask. Based on this model, the binary mask optimization algorithm is proposed for two typical kinds of optical lithography systems. Topological constraints are applied in the optimization framework to limit the minimum feature size on the mask. Simulations illustrate that our approach is effective and practical.

ACKNOWLEDGMENTS

We wish to thank Christof Krautschik, Yan Borodovsky, and the Technology Computer Aided Design group at the Intel corporation for their comments and support.

REFERENCES

1. A. K. Wong, *Resolution Enhancement Techniques* (SPIE Press, 2001).
2. S. A. Campbell, *The Science and Engineering of Microelectronic Fabrication* 2nd ed. (Publishing House of Electronics Industry, Beijing, China, 2003).
3. F. Schellenberg, "Resolution enhancement technology: The past, the present, and extensions for the future, optical microlithography," Proc. SPIE **5377**, 1–20 (2004).
4. F. Schellenberg, *Resolution Enhancement Techniques in Optical Lithography* (SPIE Press, 2004).
5. L. Liebmann, S. Mansfield, A. Wong, M. Lavin, W. Leipold, and T. Dunham, "TCAD development for lithography resolution enhancement," IBM J. Res. Dev. **45**, 651–665 (2001).
6. S. Sherif, B. Saleh, and R. Leone, "Binary image synthesis using mixed integer programming," IEEE Trans. Image Process. **4**, 1252–1257 (1995).
7. Y. Liu and A. Zakhor, "Binary and phase shifting mask design for optical lithography," IEEE Trans. Semicond. Manuf. **5**, 138–152 (1992).
8. Y. C. Pati and T. Kailath, "Phase-shifting masks for microlithography: Automated design and mask requirements," J. Opt. Soc. Am. A **11**, 2438–2452 (1994).
9. A. Erdmann, R. Farkas, T. Fuhner, B. Tollkuhn, and G. Kokai, "Towards automatic mask and source optimization for optical lithography," Proc. SPIE **5377**, 646–657 (2004).
10. L. Pang, Y. Liu, and D. Abrams, "Inverse lithography technology (ilt): What is the impact to the photomask industry?" Proc. SPIE **6283**, 62830X–1 (2006).

11. Y. Granik, "Illuminator optimization methods in microlithography," Proc. SPIE **5524**, 217–229 (2004).
12. A. Poonawala and P. Milanfar, "Mask design for optical microlithography—an inverse imaging problem," IEEE Trans. Image Process. **16**, 774–788 (2007).
13. X. Ma and G. R. Arce, "Generalized inverse lithography methods for phase-shifting mask design," Proc. SPIE **6520**, 65200U (2007).
14. X. Ma and G. R. Arce, "Generalized inverse lithography methods for phase-shifting mask design," Opt. Express **15**, 15066–15079 (2007).
15. X. Ma and G. R. Arce, "Binary mask optimization for inverse lithography with partially coherent illumination," Proc. SPIE **7140**, 71401A (2008).
16. X. Ma and G. R. Arce, "Binary mask optimization for inverse lithography with partially coherent illumination," J. Opt. Soc. Am. A **25**, 2960–2970 (2008).
17. X. Ma and G. R. Arce, "Psm design for inverse lithography using illumination with samll partial coherence factor," Proc. SPIE **7274**, 727437 (2009).
18. X. Ma and G. R. Arce, "Psm design for inverse lithography with partially coherent illumination," Opt. Express **16**, 20126–20141 (2008).
19. X. Ma and G. R. Arce, "Pixel-based simultaneous source and mask optimization," Opt. Express **17**, 5783–5793 (2009).
20. J. Tirapu-Azpiroz, P. Burchard, and E. Yablonovitch, "Boundary layer model to account for thick mask effects in photolithography," Proc. SPIE **5040**, 1611–1619 (2003).
21. J. Tirapu-Azpiroz and E. Yablonovitch, "Fast evaluation of photomask near-fields in subwavelength 193 nm lithography," Proc. SPIE **5377**, 1528–1535 (2004).
22. A. Wong, "Rigorous three-dimensional time-domain finite difference electromagnetic simulation," Ph.D. thesis (University of California, Berkeley, 1994).
23. A. Wong and A. R. Neureuther, "Mask topography effects in projection printing of phase shift masks," IEEE Trans. Electron Devices **41**, 895–902 (1994).
24. C. Pierrat, A. Wong, and S. Vaidya, "Phase-shifting mask topography effects on lithographic image quality," in *IEEE International Electron Devices Meeting*, Technical Digest (IEEE, 1992), pp. 53–56.
25. C. M. Yuan, "Calculation of one-dimension lithographic aerial images using the vector theory," IEEE Trans. Electron Devices **40**, 1604–1613 (1993).
26. K. Lucas, H. Tanabe, and A. J. Strojwas, "Efficient and rigorous three-dimensional model for optical lithography simulation," J. Opt. Soc. Am. A **13**, 2187–2199 (1996).
27. A. Erdmann, P. Evanschitzky, G. Citarella, T. Fühner, and P. D. Bisschop, "Rigorous mask modeling using waveguide and FDTD methods: An assessment for typical hyper NA imaging problems," in Proc. SPIE **6283**, 628319 (2006).
28. K. Adam and A. R. Neureuther, "Domain decomposition methods for the rapid electromagnetic simulation of photomask scattering," J. Microlithogr. Microfabr. Microsyst. **1**, 253–269 (2002).
29. B. E. A. Saleh and M. Rabbani, "Simulation of partially coherent imagery in the space and frequency domains and by modal expansion," Appl. Opt. **21**, 2770–2777 (1982).
30. M. Born and E. Wolfe, *Principles of Optics* (Cambridge U. Press, 1999).
31. R. Wilson, *Fourier Series and Optical Transform Techniques in Contemporary Optics* (Wiley, 1995).
32. B. Salik, J. Rosen, and A. Yariv, "Average coherent approximation for partially cohernet optical systems," J. Opt. Soc. Am. A **13**, 2086–2090 (1996).
33. J. Tirapu-Azpiroz, "Analysis and modeling of photomask near-fields in sub-wavelength deep ultraviolet lithography with optical proximity corrections," Ph.D. thesis (University of California, Los Angeles, 2004).
34. K. Adam, "Domain decomposition methods for the electromagnetic simulation of scattering from three-dimensional structures with applications in lithography," Ph.D. thesis (University of California, Berkeley, 2001).
35. A. Poonawala, "Mask design for single and double exposure optical microlithography: an inverse imaging approach," Ph.D. thesis (University of California, Santa Cruz, 2007).
36. L. Lam, S. W. Lee, and C. Y. Suen, "Thinning methodologies—a comprehensive survey," IEEE Trans. Pattern Anal. Mach. Intell. **14**, 869–885 (1992).
37. P. Yu and D. Z. Pan, "Tip-opc: a new topological invariant paradigm for pixel based optical proximity correction," in *Proceedings of the ACM/IEEE International Conference on Computer-Aided Design (ICCAD)* (IEEE, 2007), pp. 847–853.